Mechanism-based constitutive modeling of ZEK100 magnesium alloy with crystal plasticity and in-situ HEXRD experiment

Hyuk Jong Bong[a,*], Xiaohua Hu[b], Xin Sun[b], Yang Ren[c]

[a] Advanced Metals Division, Korea Institute of Materials Science, Changwon, Gyeongnam 51508, South Korea

[b] Energy & Transportation Science Division, Oak Ridge National Laboratory, Oak Ridge, TN 37831, USA

[c] X-ray Science Division, Argonne National Laboratory, Argonne, IL 60439, USA

*Corresponding author:

E-mail: hjbong@kims.re.kr, Tel: +82-55-280-3560, Fax: +82-55-280-3599

Abstract

The constitutive behavior of a hexagonal close-packed (HCP) polycrystalline ZEK100 magnesium alloy was investigated using combined high energy X-ray diffraction (HEXRD) from a synchrotron source and crystal plasticity modeling approach. The *in-situ* tensile test data coupled with the HEXRD enabled the tracking of the lattice strain evolution during deformation. The microscopic behavior represented by lattice strain and the macroscopic behavior represented by stress-strain curves were then used together as objective function to estimate the critical resolved shear stress (CRSS) and hardening parameters of available slip and deformation twin systems in the ZEK100 alloy. An enhanced predominant twinning reorientation (ePTR) scheme was proposed in the current work, and the ePTR parameters were determined for the first time by the use of basal plane peak intensity along loading direction measured from HEXRD. Two crystal plasticity models, the computationally efficient elastic-plastic self-consistent (EPSC) and crystal plasticity finite element (CPFE) models, were developed incorporating the deformation twinning for the HCP-structured metals. The determined constitutive parameters were further validated by comparing the predicted deformation texture with the measured one. The work provides a useful and computationally-efficient modeling scheme to understand the slip/twin induced deformation behaviors of the ZEK100 alloy in micro- and macro-scales.

Keywords: Crystal plasticity finite element; Elastic-plastic self-consistent model; Deformation twin; Magnesium alloy; High-energy X-ray diffraction

1. Introduction

The recent decade has witnessed a world-wide increase in the use of magnesium alloys as structural materials for lightweighting vehicles due to their high strength-to-density ratio (Lee et al., 2017). However, wrought magnesium alloy sheets possess strong basal texture after rolling, leading to poor formability due to the limited number of slip systems that can be activated at room temperature, which hinders the more rapid and broad applications of the magnesium sheets in vehicle body applications (Kurukuri et al., 2014). Although formability can be improved at elevated temperatures (Bong et al., 2013), it requires complex tooling and lubrication strategies, which increase production cost. A plausible strategy in improving the room temperature formability of the magnesium alloy has been the addition of rare-earth elements such as Ce, Nd, Y, and Gd, which can weaken the basal texture (Al-Samman and Li, 2011; Bohlen et al., 2007; Jiang et al., 2011; Kurukuri et al., 2014). The controlled texture characteristics by adding the rare-earth elements could lead to enhanced formability relative to typical commercial AZ31 alloy (Bohlen et al., 2007). In particular, ZEK100 alloy, a typical magnesium alloy with rare-earth element added, has been successfully formed at temperatures considerably lower than those required for AZ31 (Boba, 2014). The material has been of a considerable interest, and it is crucial to establish the quantitative and mechanism-based understandings between the microstructural characteristics of the material and the macroscopic mechanical properties.

Various meso-scale crystal plasticity models have been reported in the open literature on the constitutive modeling of magnesium sheet alloys considering the deformation anisotropy caused by the grain-level deformation heterogeneities induced by the texture, and the critical resolve shear stress (CRSS) ratio between available slip/twin systems (Agnew et al., 2018, 2003; Ardeljan et al., 2016; Liu et al., 2018, 2017; Liu and Wei, 2014; Ma et al., 2017; Qiao et al., 2016, 2015; Singh et al., 2018; Tadano et al., 2016; Wang et al., 2018, 2012b, 2012a, 2010a; Wang et al., 2013b; Zhang and Joshi, 2012) deformation mechanisms. For instance, Tomé et al. (1991) proposed predominant twin reorientation (PTR) model to explicitly capture the deformation twining kinematics, and the model has been frequently adopted in other studies (Liu et al., 2017; Ma et al., 2017; Tomé et al., 1991; Wang et al., 2013b; Wang et al., 2012a, 2012b). Simpler form of empirical equation was also proposed to model the twinning kinematics (Guo et al., 2015; Qiao et al., 2016). Furthermore, during the last several years, researchers also have focused on the mechanical responses of magnesium alloys under cyclic loading or complex loads considering the so-called twinning and de-twinning phenomena (Guo

et al., 2015; Nemcko et al., 2017; Proust et al., 2009; Qiao et al., 2017, 2015; Wang et al., 2013; Wu et al., 2008)

To enable accurate prediction of material's behavior using the crystal plasticity modeling, accurate identification of the constitutive parameters for the various plastic deformation mechanisms such as dislocation slips or deformation twinning are vital. However, accurate characterization of the constitutive parameters for each deformation mechanism is challenging due to the lack of direct measurement techniques. Furthermore, multiple sets of constitutive parameters for each slip (and/or twinning system) or for each phase of multi-phase metals can be determined by back-fitting to 'macroscopic' stress-strain behavior.

A simple example of the case can be seen from representative volume element (RVE) modeling for dual-phase steels where the phase properties of ferrite and martensite were determined by fitting to uniaxial stress-strain curve of dual-phase composite (Govik et al., 2014; Ha et al., 2014). Recently, Bong et al. (2017) pointed out that determined phase properties for the ferrite and martensite are not unique, and they can lead to a wide range of uncertainties in predicting the independent macroscopic behavior such as Baushinger effect (Govik et al., 2014; Ha et al., 2014). Such problem is exacerbated particularly for multi-phase materials and materials possessing low-symmetric slip (and/or twin) systems such as HCP metals.

A plausible approach to accurately characterize the constitutive behaviors of the HCP metals is to quantify the constitutive parameters at the microstructural scale, for instance, lattice strain. *In-situ* measurement using high-energy X-ray diffraction (HEXRD), whose typical energy is orders of magnitude higher than conventional X-ray, on a sample can provide opportunities to identify the unique set of the constitutive parameters for the multiple slip/twin systems[1]. The HEXRD enables the volumetric diffraction measurement by penetrating the entire sheet metal thickness, typically in millimeter length scale (Hu et al., 2017; Sun et al., 2009)[2]. During *in-situ* HEXRD experiments, the diffraction pattern changes, which indicate microstructural

[1] It should be clarified that "High Energy" is only relevant to greater penetration depth compared with the conventional X-ray, but not higher resolution since diffraction angle by HEXRD is smaller than that by conventional XRD.

[2] Recently, a new experimental technique to enable transmission-based X-ray measurement by using conventional Cu-K_α and polycapillary optic was devised. Although the sample must be thin (<0.7 mm) to permit X-ray penetration, the new device could enlarge the beam length to several millimeters, and consequently, provides better grain statistics. Interested readers are directed to Refs. (Kada et al., 2016, 2015).

changes of the material, are continuously recorded while the sample undergoes mechanical loading such as a uniaxial tension. By such means, the microscopic lattice strain changes of lattice planes can be calculated with the diffraction patterns, and they can be correlated with the macroscopic stress-strain behaviors. Similar approach can be made using neutron diffraction method, however, with a much lower throughput compared with the HEXRD. The *in-situ* neutron diffraction measurement, in which the loading should be interrupted due to its long collection times (Gnäupel-Herold, 2009; Wang et al., 2012b), can be complicated by stress relaxation effect. To overcome this shortcoming, there have been several studies that account for the stress (or strain) relaxation effect numerically in crystal plasticity models (Wang et al., 2013a; Wang et al., 2016). Recently, Wang et al. (2016) implemented such effects in Elastic-Visco-Plastic polycrystal (EVPSC) framework by postulating a resolved shear stress distribution acting on each slip/twin plane and correlating the distribution with dislocation density. Finally, they reproduced the stress (or strain) relaxation associated with the strain (or stress) holds. On the other hand, HEXRD can enable the continuous diffraction measurement during loading without stopping if sufficiently low loading speed is imposed. Therefore, special treatment to address the stress relaxation effect is not required for the HEXRD from the modeling perspective (Wang et al., 2012b).

The aforementioned HEXRD approach (or neutron diffraction) has been coupled with crystal plasticity models such as elastic-plastic self-consistent (EPSC), elastic-viscoplastic self-consistent (EVPSC), and finite element-based crystal plasticity (hereafter, referred as 'CPFE') models to study the micromechanical behavior such as lattice strain changes for multiphase metals (Cong et al., 2009; Hu et al., 2016, 2017; Jia et al., 2009) and for HCP-structured metals (Abdolvand et al., 2011; Agnew et al., 2018, 2013, 2006, 2003, Lentz et al., 2015, 2014; Muránsky et al., 2008; Neil et al., 2010; Wang et al., 2018, 2012b; Wang et al., 2013b; Wu et al., 2008). In these approaches, the simulations were seeded with initial grain orientations measured from the diffraction experiments, and the microstructural-level constitutive parameters, i.e., CRSS and hardening parameters of the various slip or twin systems, were calibrated by iterative fitting to either the stress-strain response or the lattice strain evolution (hereafter, the method is referred to as the 'trial-and-error' approach). Although the EPSC (or EVPSC) framework is time-efficient as compared with the CPFE scheme, it ignores spatial distribution of the individual grain and the grain to grain interaction. On the contrary, the modern CPFE modeling can provide a greater degree of modeling fidelity to explicitly account for the intragranular stress variation and the grain-grain interactions. However, the CPFE

simulations are orders of magnitude slower than the EPSC simulations by explicitly resolving the grains orientations in the FE meshes. This shortcoming has been hindering the application of the CPFE model to determine the myriad constitutive parameters for HCP metals with multiple slip and twin systems. Recently, Hu et al. (2017) developed a computationally-efficient CPFE modeling procedure in conjunction with the EPSC model. In their work, the EPSC model was first used to roughly estimate the constitutive parameters for four different phases in a QP980 steel. The EPSC-determined parameters were then used in the CPFE simulation as an initial estimation, and refinement of the parameters were followed to improve the prediction accuracy of the CPFE model. Using the new scheme, the multiple parameters were readily determined for the CPFE model, and thus, the approach could fill the gap between the EPSC and CPFE modeling.

In the current study, both micro- and macro-mechanical properties of the twin-roll casted ZEK100 alloys were investigated. The *in-situ* HEXRD experiments were conducted during the uniaxial tension tests along the rolling direction (RD) and the transverse direction (TD) to measure the lattice strain evolutions and stress-strain behaviors. Newly developed crystal plasticity models, i.e., EPSC and CPFE, for the HCP-structured metal by incorporating the deformation twinning mechanisms were coupled with the HEXRD measurements. The CRSS and hardening parameters of the available slip and twin systems were determined following the procedure described by Hu et al. (2017). Furthermore, efforts were also made to explicitly capture the deformation twinning kinematics utilizing the PTR model (Tomé et al., 1991).

The originality of the current work is rich in the following aspects: (a) It closely ties the micro- and macro-behaviors of ZEK 100 with computationally-efficient CPFE in conjunction with *in-situ* HEXRD. There have been limited previous research utilizing the crystal plasticity models to characterize the constitutive behaviors of ZEK100 alloys (Bohlen et al., 2007; Habib et al., 2017; Nemcko et al., 2017) but their micro-to-macro linkage was weak since the constitutive parameters were determined by back-fitting only to the macroscopic stress-strain behavior, and the determined parameters were not fully validated at the micro-scale data such as lattice strain. (b) the computationally-efficient coupled EPSC and CPFE modeling approach is applied to HCP-structured metals for the first time, and (c) a direct comparison of twinning rates between experiments and simulations are provided using the PTR model and an enhanced PTR (ePTR) modeling scheme is proposed to better capture the deformation twinning rate.

The remainder of this paper is organized as follows. The microstructural and mechanical properties of the ZEK100 determined from the *in-situ* HEXRD experiments are described in Section 2. In Section 3, theoretical background of the newly developed crystal plasticity models for the HCP metals are presented. In Section 4, the results of crystal plasticity simulations are compared with the experimental data and discussed.

2. Experimental procedures and results

Twin-roll casted ZEK100 magnesium alloy with thickness of 1.5 mm produced by POSCO was investigated. The chemical composition of the ZEK100 is listed in Table 1.

Table 1 Chemical composition of ZEK100 in wt%

Mg	Zn	Ce	La	Zr
Balance	1.3	0.1	0.1	0.5

2.1 *In-situ* HEXRD tensile test

The schematic of the experimental setup for *in-situ* loading studies using the synchrotron-based HEXRD is shown in Figure 1 (a). The experiments were performed at the 11-1D-C of the Advanced Photon Source (APS) at Argonne National Laboratory. The wavelength λ of the beam was 0.01173 nm. Sub-sized tensile samples with the sheet thickness of 1.5 mm, depicted in Figure 1 (b), were mounted to a loading frame. Nearly square-shaped incident X-ray beam of 500 μm × 500 μm impinged the center of the sample during the test. The energy of the X-rays was high enough to penetrate through the 1.5 mm thick ZEK 100, and the entire transmission geometry was used for the investigation[3]. The incident beam was assumed to diffract as it penetrates the sample following the Bragg's law:

$$2d_{hkil}\sin\theta_{hkil} = \lambda \tag{1}$$

where *hkil* are the Miller-Bravais indices (throughout the paper, the Miller-Bravais notation will be used for the HCP system) of the lattice plane, therefore, d_{hkil} and θ_{hkil} are the lattice spacing and diffraction angle of the $\{hkil\}$ planes, respectively.

[3] The grain size of the ZEK100, which contains zirconium as a grain refiner, is generally known to be small (<20 μm). Given the HEXRD measurement volume (i.e., 500 μm × 500 μm × 1500 μm) that the number of grains within such volume would be more than ~47,000, and it should be sufficient to generate Debye ring.

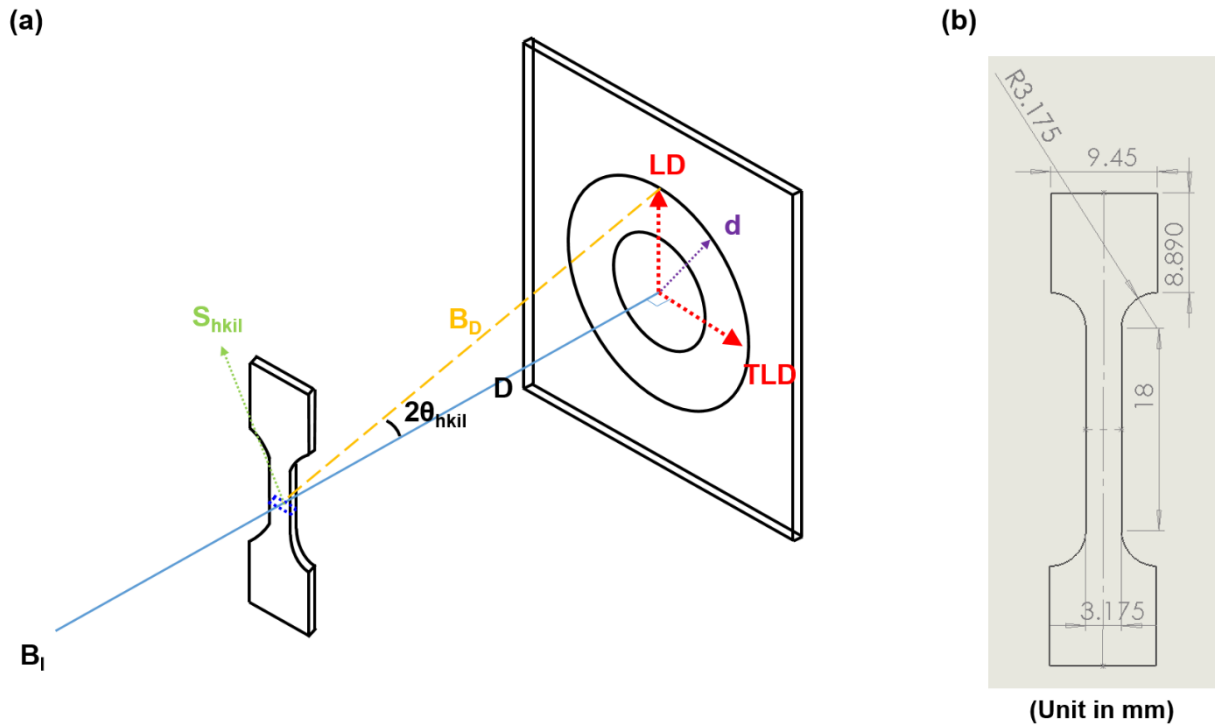

Figure 1. (a) Schematic of experimental setup for *in-situ* loading studies by synchrotron-based HEXRD (Hu et al., 2017), where B_I and B_D are incident and diffracted beams, and S_{hkil} is the diffraction vector (note: LD=loading direction; TLD=transverse direction relative to loading direction; D=distance from sample to the area detector; d=a vector from the center of the Debye ring), and (b) uniaxial tensile sample geometry with thickness of 1.5 mm.

The custom-built tensile frame with the loading capacity of 13 kN was used for the tensile test of the sub-sized sample with 18 mm were first measured as the sample was rotated from 0 to 90° along the LD, in order to characterize the texture of the undeformed ZEK100 before the tensile test. The tensile tests were conducted at room temperature at a constant grip speed of 5 µm/s, which led to approximately the nominal strain rate of 10^{-4} s^{-1}. The quasi-static nominal strain rate enabled the *in-situ* diffraction measurement without interrupting the tests, eliminating effects of stress relaxation[4]. The sample was positioned such that one of the planar surface (LD × TLD) was normal to the incident beam during the *in-situ* tensile test. Tensile tests along two directions, RD and TD, were conducted.

[4] Usual HEXRD data collection time duration is ~1 s (two 0.5 s sub-frames). Considering the grip speed of 5 µm/s and X-ray beam spot length (~500 µm), the error cause by deformation during the measurement would be negligible.

During the tensile test, the tensile load (F) was obtained from the voltage signal from the load cell equipped in the tensile frame, and displacement (ΔL) of the tensile frame were recorded. The load and displacement can be used to calculate the engineering stress (S)-strain (e) behavior as follows:

$$S = \frac{F}{A_0},\ e = \frac{\Delta L}{L_0} \tag{2}$$

where initial cross-sectional area (A_0) and gauge length (L_0) of the tensile sample are 1.5 mm × 3.175 mm and 18 mm, respectively. The stiffness correction procedure outlined in Hu et al. (2016, 2017) was followed to compensate for the insufficient stiffness of the tensile frame.

2.2 Initial texture

From the HEXRD measurement, 2-dimensional Debye ring image could be obtained (see Figure 2 (a)) as an example with the corresponding lattice planes of each ring. Similar as described by Hu et al. (2017), initial texture was measured before tensile test by rotating the sample along the loading direction (LD) from 0° to 90°. During the tensile loading the Debye diffraction rings were collected incrementally with an interval of 4°. Then the fit2D software (Hammersley, 2004) was used to analyze the collected Debye rings. With a novel correction approach proposed by Hu et al. (2018, 2017), which accounts for both incident beam intensity variation and sample thickness changes during the rotation. The $\{10\bar{1}0\}$, $\{0002\}$, and $\{11\bar{2}0\}$ pole figures were calculated from the fit2D analyzed data.

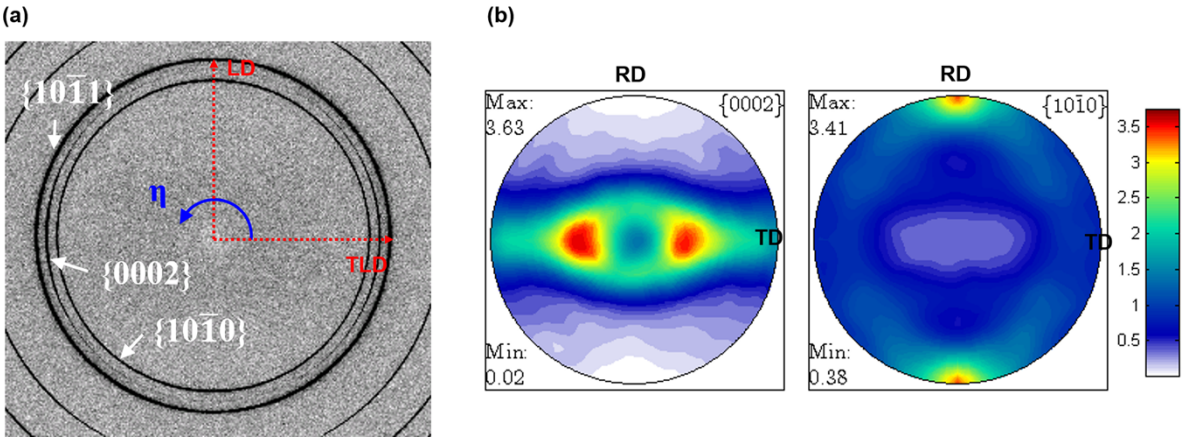

Figure 2. (a) Debye rings image of the ZEK100 before the tensile loading from the HEXRD measurement, and (b) initial texture of ZEK100 represented in terms of the $\{0002\}$ and $\{10\bar{1}0\}$ pole distributions

The obtained pole figures were then analyzed to estimate the orientation distribution function (ODF) using MTEX software (Hielscher and Schaeben, 2008). The coefficients of the ODF to minimize error between the experimentally collected and MTEX-calculated pole figures were calibrated using a least square fitting. For the analysis presented here, the de la Valle-Poussin kernel and 5° half width were used. The MTEX-calculated basal $\{0002\}$ and prismatic $\{10\bar{1}0\}$ pole figures of the undeformed sample are shown in Figure 2 (b). The ZEK100 exhibits very weak basal texture, and the c-axis (basal plane normal) of grains are mostly aligned perpendicular to the RD. The basal poles are spread along the TD-ND plane, and two major peaks are aligned ±25° from the ND to the TD, approximately. Similar texture characteristics were also observed for the same alloy system in Abedini et al. (2017)[5].

2.3 Lattice strain

During tensile loading, the intensity peaks continuously shift due to the lattice distortion, and the lattice strains can be calculated by analyzing the peak shift. The angle η shown in Figure 2 (a) is defined as the angle from the TLD along the counterclockwise direction. In order to calculate the lattice strains along the LD, the intensities were only integrated along the arc with η=88-92° (denoted by $I_{88\text{-}92}$). The $I_{88\text{-}92}$ was also calculated as a function of 2θ for each measurement point from the HEXRD during the tensile loading. The $I_{88\text{-}92}$ vs. 2θ plots of an undeformed sample and deformed sample with tensile strain of 0.1 along the RD are shown in Figure 3 as a typical example.

[5] As will be shown later, a noticeable deformation twinning is activated in the investigated ZEK100 during the uniaxial tension along TD, and thus, the deformation twinning can be characterized by utilizing the mechanical data in such loading condition. Note that, common AZ31 with basal texture essentially requires in-plane compression test for the twinning characterization. Given the fact that only the tensile tester for sheet metals is equipped with the current HEXRD set-up at Argonne National Lab, the ZEK100 material was selected for the investigation in this study.

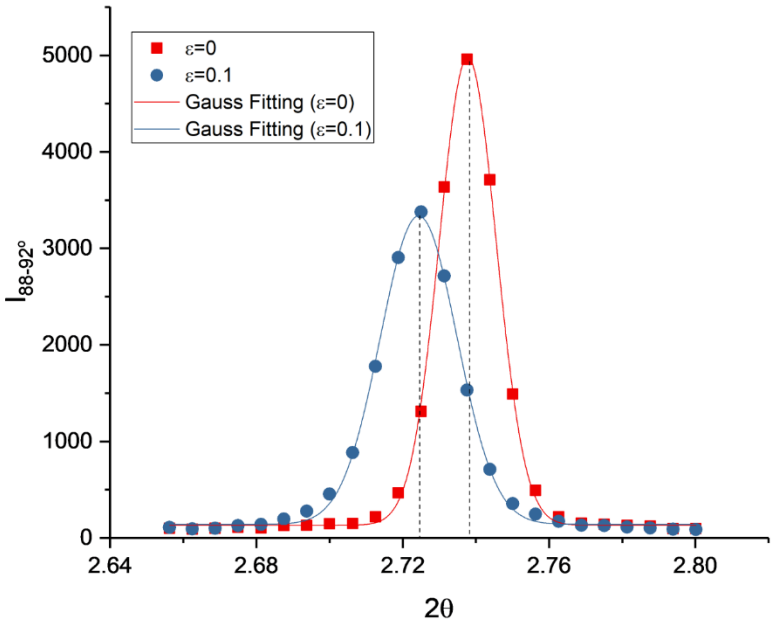

Figure 3. $I_{88\text{-}92}$ vs. 2θ plots of an undeformed sample and a deformed sample with a tensile strain of 0.1 along the RD for the $\{10\bar{1}0\}$ lattice plane peak (ε denotes macroscopic tensile strain along the LD)

Intensity peaks were then fitted using Gausian distribution functions by OriginPro 2017 software (Edwards, 2002) to determine the θ_{hkil} for each strain step. Following the previous works (Hu et al., 2016, 2017; Jia et al., 2009), the lattice strains of *{hkil}* lattice plane, ε^{L}_{hkil}, were calculated in true strain notation as follows:

$$\varepsilon^{L}_{hkil} = \ln\frac{d^{\varepsilon}_{hkil}}{d^{\varepsilon=0}_{hkil}} = \ln\frac{\sin\theta^{\varepsilon=0}_{hkil}}{\sin\theta^{\varepsilon}_{hkil}} \tag{3}$$

where superscript ε denotes the (macroscopic) tensile strain along the LD.

The lattice strain along the LTD could be also calculated following the foregoing procedures with η ranging from -2 to 2° for the intensity integration. The lattice strains were calculated for the tension along the RD and TD. Finally, the sets of lattice strains along two measurement directions, the LD and LTD, under the two tensile loading directions, the RD and TD, were obtained.

3. Modeling

3.1 Elastic-plastic self-consistent (EPSC) model

In the current study, the original release of the EPSC code by Turner and Tomé (1994) (Turner and Tomé, 1994), which does not account for the grain re-orientation associated with slip, was used. Note that there are available recent versions of EPSC (Neil et al., 2010) or EVPSC code (Wang et al., 2010b) which account for the slip-associated grain re-orientation. In the EPSC model, each crystallographic orientation (or grain) with its instantaneous modulus of L_g is treated as an ellipsoidal elasto-plastic inclusion embedded in a homogeneous effective medium with overall moduli L. The homogeneous effective medium reproduces the overall response of the polycrystal, with anisotropic properties specified by a set of discrete Euler angles weighted to reproduce the overall texture. The model addresses the deformation heterogeneity of each ellipsoidal grain of different crystallographic orientations by solving the Eshelby ellipsoidal inclusion problem (Eshelby, 1957). The interaction equation linking the microscopic strain rate tensor at the grain scale $\dot{\boldsymbol{\varepsilon}}_g$ and the macroscopic strain rate tensor of the polycrystalline $\bar{\dot{\boldsymbol{\varepsilon}}}$ is derived as follows:

$$\dot{\boldsymbol{\varepsilon}}_g = A_g \bar{\dot{\boldsymbol{\varepsilon}}} \tag{4}$$

with A_g expressed as

$$A_g = \left(L^* + L_g\right)^{-1}\left(L^* + L\right) \tag{5}$$

where L^* is a constraint tensor for a matrix containing an ellipsoidal inclusion with same orientation and the shape as the grain. At each time step, constitutive equation for the single crystal and the self-consistent criteria are simultaneously solved. By such means, the interaction of the grain inclusions with the medium can be accounted for.

Here, the generalized Voce law was adopted to describe the strain induced instantaneous CRSS variations of α^{th} slip system, $\tau_c^{(\alpha)}$, as follows:

$$\tau_c^{(\alpha)} = \tau_0^{(\alpha)} + \left(\tau_1^{(\alpha)} + \theta_1^{(\alpha)} \cdot \Gamma\right)\left[1 - \exp\left(-\frac{\theta_0^{(\alpha)} \cdot \Gamma}{\tau_1^{(\alpha)}}\right)\right] \tag{6}$$

where $\Gamma = \sum_{\alpha=1}^{N^{SL}} \left|\gamma^{(\alpha)}\right|$ is the total accumulated shear strain for all slip systems over the deformation history, where N^{SL} is total number of slip systems. $\tau_0^{(\alpha)}$, $\tau_1^{(\alpha)}$, $\theta_0^{(\alpha)}$, and $\theta_1^{(\alpha)}$ are the initial CRSS, the difference between saturation and initial yield, the initial hardening rate, and the linear hardening rate, respectively. The linear hardening term, $\theta_1^{(\alpha)} \cdot \Gamma$, controls the hardening rate at large strain. The evolution of $\tau_c^{(\alpha)}$ in time derivative form is given by:

$$\dot{\tau}_c^{(\alpha)} = \frac{d\tau_c^{(\alpha)}}{d\Gamma} \sum_{i=1}^{N^{SL}} \boldsymbol{h}_{ij} \dot{\gamma}^{(j)} \tag{7}$$

where $\boldsymbol{h}_{ij}$ is a hardening coefficient represented by

$$\boldsymbol{h}_{ij} = h_j \left(q + (1-q)\delta_{ij} \right) \tag{8}$$

where q is the ratio of the 'latent' hardening rate to the 'self' hardening rate, and δ_{ij} is Kronecker delta. Since 'self' and 'latent' hardenings could not be distinguished in the diffraction data, a value of 1.0 was used for all components of $\boldsymbol{h}_{ij}$ for all the slip systems considered here.

An incremental stress boundary condition was applied for the uniaxial tension. The calculation described above was iteratively performed until self-consistency condition was achieved between the average response of the homogeneous medium and that of the individual grains from which the average response was calculated. The set of hardening parameters for each slip (and twin) system was identified by fitting to the experimental macroscopic stress-strain curves and the microscopic lattice strain variation, simultaneously, using the iterative trial-and-error approach.

3.2 Crystal plasticity finite element (CPFE) modeling

The description below is intended to provide sufficient background to understand the CPFE model and its particular implementation in the current work in brief sense. Interested readers are directed to the details on mathematical formulations (Kalidindi, 1992; Kalidindi et al., 1992) and other modifications within the original framework (Bong, 2017; Bong et al., 2018; Gan et al., 2017; Kim et al., 2017; Lim et al., 2018).

The shear rate on the slip system α is generally expressed according to (Kalidindi et al., 1992)

$$\dot{\gamma}^{(\alpha)} = \dot{\gamma}_0 \left(\frac{\tau^{(\alpha)}}{\tau_c^{(\alpha)}} \right)^{(1/m)} sign\left(\tau^{(\alpha)} \right) \tag{9}$$

where $\dot{\gamma}_0$ denotes a reference shear rate, $\tau^{(\alpha)}$ is the resolved shear stress of the α^{th} slip system, and m represents the strain rate sensitivity exponent. $\dot{\gamma}_0$ and m were set as 0.0001 s^{-1} and 0.02, respectively. The extended Voce hardening law expressed in Eqs. (6)-(8) used for the EPSC model was also adopted to model $\tau_c^{(\alpha)}$ in the CPFE model. The model described above

is implemented in ABAQUS user subroutine following previous studies (Kalidindi, 1992; Kalidindi et al., 1992).

3.3 Modeling consideration of deformation twinning

The foregoing subsections complete the basic formulation for the EPSC and CPFE without the consideration of the deformation twinning kinematics. This subsection presents the additional treatment to account for the deformation twinning in the two crystal plasticity models. A brief review in previous research works (Abdolvand et al., 2011; Agnew et al., 2006; Ardeljan et al., 2016; Kalidindi, 1998; Muhammad et al., 2015; Muránsky et al., 2009, 2008; Tadano et al., 2016; Wang et al., 2012b; Wang et al., 2013; Wang et al., 2012a; Zhang and Joshi, 2012) will provide the essential perspective on this subject.

For the modeling purpose, the deformation twinning was assumed to be essentially pseudo slip that obeys Schmid law (Abdolvand et al., 2011; Ardeljan et al., 2016; Kalidindi, 1998; Liu et al., 2017; Tadano et al., 2016; Wang et al., 2013; Wang et al., 2012a, 2012b; Zhang and Joshi, 2012). Note that the tensile twinning was found to obey the Schmid law from previous neutron diffraction studies (Brown et al., 2005; Gharghouri et al., 1999). The instantaneous CRSS variation for the deformation twin also follows the generalized Voce law expressed in Eqs. (6)-(8), therefore, Eq. (6) to represent the τ_c of β^{th} twin variants[6] becomes as follows:

$$\tau_c^{(\beta)} = \tau_0^{(\beta)} + \left(\tau_1^{(\beta)} + \theta_1^{(\beta)} \cdot \Gamma\right)\left[1 - \exp\left(-\frac{\theta_0^{(\beta)} \cdot \Gamma}{\tau_1^{(\beta)}}\right)\right] \tag{10}$$

The total accumulated shear strain Γ is expressed as,

$$\Gamma = \sum_{\alpha=1}^{N^{SL}} \left|\gamma^{(\alpha)}\right| + \sum_{\beta=1}^{N^{TW}} \left|\gamma^{(\beta)}\right| \tag{11}$$

where N^{SL} and N^{TW} are total number of slip systems and twin variants, respectively.

The evolution of $\tau_c^{(\alpha)}$ becomes as follows:

$$\dot{\tau}_c^{(\alpha \text{ or } \beta)} = \frac{d\tau_c^{(\alpha \text{ or } \beta)}}{d\Gamma} \sum_{i=1}^{N^{SL}+N^{TW}} h_{ij} \dot{\gamma}^{(j)} \tag{12}$$

Current twin volume fraction f^{β} in a grain is assumed to evolve as follows:

---

[6] To avoid a confusion with the slip systems, superscript 'β' is used for the twin variants throughout the paper.

$$\dot{f}^{(\beta)} = \frac{\dot{\gamma}^{(\beta)}}{\gamma^{TW}} \tag{13}$$

where γ^{TW} is tensile twinning shear determined by the aspect ratio of crystal lattice, $\chi=c/a$ (1.624 for magnesium) as follows (Yoo, 1981):

$$\gamma^{TW} = \frac{\sqrt{3}}{\chi} - \frac{\chi}{\sqrt{3}} \quad \{10\bar{1}2\}<\bar{1}011> \quad \text{(for tensile twin)} \tag{14}$$

Since the compressive twin is known to rarely happen in magnesium alloys (Staroselsky, 1998) with its very high CRSS, it is not considered. Only the positive resolved shear stress is allowed to account for the polar nature of twinning (Kalidindi, 1998; Zhang and Joshi, 2012).

Grain re-orientation is introduced when the accumulated twin volume fraction exceeds the threshold value f_{cr} at an integration point (Note that the EPSC does not consider the grain re-orientation associated with slip, but abrupt re-orientation due to twinning is considered for the current model). Widely used PTR model (Liu et al., 2017; Tomé et al., 1991; Wang et al., 2013; Wang et al., 2012a, 2012b) is adopted in this study with further modification, which will be discussed later (other forms of empirical equation for f_{cr} are also available. Therefore, interested readers are directed to the details in Refs. (Guo et al., 2015; Qiao et al., 2016)). It has been reported that the deformation twinning occurs on a twin variant with the highest resolved shear stress in various materials (Chin et al., 1969; Gharghouri et al., 1999). Therefore, only one twin variant with the highest resolved shear stress among possible twin variants was allowed to be activated in the PTR model, and f_{cr} evolves in a grain as follows:

$$f_{cr} = A + B\frac{F_E}{F_R} \tag{15}$$

where A and B are material constants, and they control the twinning rate during the early deformation stage and during middle of the deformation as grains start to be fully twinned, respectively. F_E and F_R denote volume fraction of fully twinned grains and volume fraction of twinned region over all grains, respectively, and the two variables can be mathematically expressed as follows:

$$F_E = \sum_{m=1}^{NG^{twinned}} w^m \Big/ \sum_{n=1}^{NG} w^n, \quad F_R = \sum_{n=1}^{NG} w^n \sum_{\beta=1}^{N^{TW}} f^{\beta} \tag{16}$$

where *NG* is total number of grains assumed in the simulations, $NG^{twinned}$ is the total number of fully twinned grains whose twin volume fraction exceeds f_{cr}. w represents fraction of corresponding grain over polycrystalline.

In the current study, the original version of the PTR model in Eq. (15) is further modified by including an exponent term, *C*, as follows:

$$f_{cr} = A + B\left(\frac{F_E}{F_R}\right)^C \tag{17}$$

The equation above reduces to its original version if C=1. The rationale behind the modification is relevant to the discrepancy between HEXRD measured and simulated twinning rates as will be further discussed in Section 4.4.

Once the twin volume fraction reaches f_{cr} the whole grain is completely reoriented by a transformation matrix, $\boldsymbol{Q}$, between the lattice orientation in the matrix to that in the twinned region:

$$\boldsymbol{Q} = \boldsymbol{I} - 2\boldsymbol{n} \otimes \boldsymbol{n} \tag{18}$$

where $\boldsymbol{I}$ is identity tensor, and $\boldsymbol{n}$ represents the twin plane normal vector. The new lattice orientation is determined by the twin variant which has the highest contribution to the total twin volume fraction.

The formulations described above were implemented in the EPSC and CPFE models. For the CPFE model, following the approach proposed by Kalidindi [44], the evolution of plastic deformation gradient accounting for the contributions from the deformation twinning in the untwinned region is represented as follows:

$$\mathbf{L}^p = \left(1 - \sum_{\beta=1}^{N^{TW}} f^\beta\right) \sum_{\alpha=1}^{N^{SL}} \dot{\gamma}^\alpha \left(\mathbf{s}_0^{(\alpha)} \otimes \mathbf{n}_0^{(\alpha)}\right) + \sum_{\beta=1}^{N^{TW}} \dot{f}^\beta \gamma^{TW} \left(\mathbf{s}_0^{(\beta)} \otimes \mathbf{n}_0^{(\beta)}\right) \tag{19}$$

where $\mathbf{s}_0^{(\beta)}$ and $\mathbf{n}_0^{(\beta)}$ represent twin plane normal and direction, respectively. The Cauchy stress tensor in the grain is equal to the volumetric average of stresses in the matrix and twinned regions as follows:

$$\boldsymbol{\sigma} = \left(1 - \sum_{\beta=1}^{N^{TW}} f^\beta\right) \boldsymbol{\sigma}^{Matrix} + \sum_{\beta=1}^{N^{TW}} f^\beta \boldsymbol{\sigma}^\beta \tag{20}$$

where σ^{Matrix} and σ^{β} denote the Cauchy stress tensors in the matrix and the twinned regions, respectively.

4. Results and discussion

Following the previous studies on magnesium alloys (Tadano et al., 2016; Wang et al., 2013; Wang et al., 2012a, 2012b), three slip systems and one twin system were considered: (a) $\{0001\}<11\bar{2}0>$ basal slip, (b) $\{10\bar{1}1\}<11\bar{2}0>$ prismatic slip, (c) $\{11\bar{2}2\}<11\bar{2}3>$ pyramidal slip <a+c>, and (d) $\{10\bar{1}2\}<\bar{1}011>$ tensile twin. The elastic stiffness constants for magnesium crystal, C_{11}=58, C_{12}=25, C_{13}=20.8, C_{33}=61.2, C_{44}=16.6 GPa, were adopted from literature (Staroselsky, 1998). The initial crystallographic texture of the ZEK100 data shown in Figure 2 (b) is discretized into 24,000 orientations and used for both crystal plasticity models.

The CPFE simulation was conducted using ABAQUS/standard v6.11 (ABAQUS, 2011). A 3D array of grain assemblies having 24,000 FEs of C3D8R (8-node brick element with reduced integration point) type for the uniaxial tension is shown in Figure 4 (a). Each FE represents a single grain, therefore, 24,000 (120×20×10) discrete crystallographic orientations are assigned in total. The model with the similar length ratio along the X, Y, and Z directions of the actual tensile sample used in the *in-situ* HEXRD experiment, 12:2:1, is developed to represent arbitrary location of the actual tensile sample in the gauge area. A prescribed displacement boundary condition with a constant velocity, approximately equivalent to a strain rate of 10^{-4}/s, is imposed on the positive X plane along the positive X direction. The nodes on the X plane in the other side are fixed in all directions. No constraints along the Y and Z directions are imposed, therefore, necking can appear anywhere as shown in Figure 4 (b).

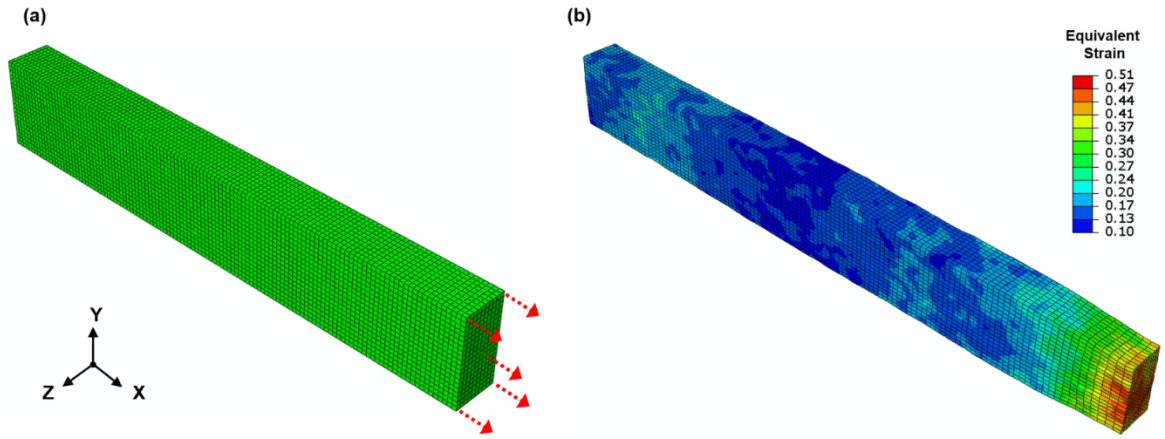

Figure 4. FE model with 24,000 grains (a) undeformed sample, and (b) deformed sample at the onset of localized necking

For both EPSC and CPFE, the macroscopic stress and strain tensors, $\boldsymbol{\sigma}$ and $\boldsymbol{\varepsilon}$, respectively, were calculated by averaging the corresponding values over all grains as follows:

$$\boldsymbol{\sigma} = \bar{\boldsymbol{\sigma}} = \frac{1}{NG}\sum_{n=1}^{NG} w^n \boldsymbol{\sigma}^n / NG, \quad \boldsymbol{\varepsilon} = \bar{\boldsymbol{\varepsilon}} = \frac{1}{NG}\sum_{n=1}^{NG} w^n \boldsymbol{\varepsilon}^n / NG \tag{21}$$

where NG denotes total number of grains assumed in the crystal plasticity models, and $\boldsymbol{\sigma}^n$ and $\boldsymbol{\varepsilon}^n$ are stress and strain tensors of n^{th} grain.

From the EPSC and CPFE predictions, the lattice strains were calculated in averaging sense using the elastic strain tensors of each crystallite. In order to calculate the lattice strain along the LD, the principal strain components along the LD of crystallites whose lattice plane normal was within the tolerance, η=88-92°, were averaged. The lattice strain along the TLD was also calculated in the same manner with the tolerance of η=-2-2°.

4.1 EPSC and CPFE models

The EPSC model was first used to determine the CRSS and hardening parameters of assumed slip/twin systems by fitting to measured stress-strain behavior and the lattice strain variation of the ZEK100 under uniaxial tension along the RD and TD, simultaneously. By such means, the micro- and macro-behaviors could be closely tied, which is non-trivial for HCP metals possessing non-symmetric slip and twin systems. Stress-strain and lattice strain data up to uniform elongation, 8.4% for the RD tension and 20.8% for the TD tension, was used for the fitting. The decision on this fitting range was made upon consideration of the spot-type beam of the HEXRD which cannot illustrate the material's behavior inside the necking area. The

determined constitutive parameters are listed in Table 2. The same set of constitutive parameters were then employed in the CPFE simulations as a first estimate. The predicted stress-strain curves using the two models are shown in Figure 5 along with the *in-situ* HEXRD data. The results show that both models well predict the anisotropic yield stresses and hardening behaviors along the two different loading directions, i.e., higher yield stress under the tension along the RD, and faster strain hardening under the tension along the TD. However, the results reveal that the CPFE model overpredicts in overall, ~3% and ~6% of the stresses for the RD and TD tensions, respectively, than EPSC model does. The differences in stress are mainly observed in two different regimes as indicated in the figure: (a) very early stage of deformation during which elastic-plastic transition is supposed to occur, and (b) later stage of the deformation, and the differential between models gets larger at larger strain. The constitutive parameters related to the two regimes are θ_0 and θ_1, respectively. The fact inspired a simple method to refine the constitutive parameters for the CPFE model, and the refined results will be presented in the next section.

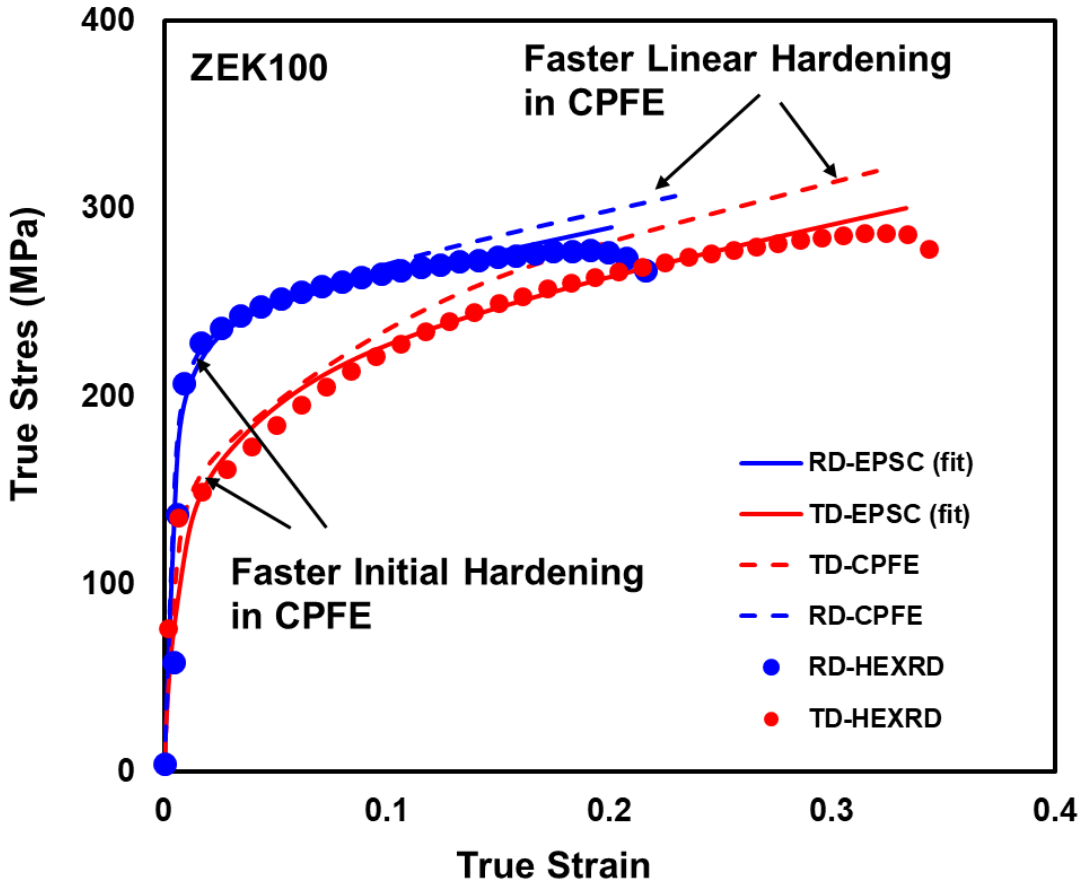

Figure 5. Stress-strain response of ZEK100 under uniaxial tension along the RD and TD.

Table 2 Best-fit constitutive parameters of slip/twin systems for ZEK100 via EPSC model

		Extended Voce parameters (Eq.(6))				PTR parameters (Eq.(17))		
	Slip/Twin System	τ_0^{EPSC} (MPa)	τ_1^{EPSC} (MPa)	θ_0^{EPSC} (MPa)	θ_1^{EPSC} (MPa)	A^{EPSC}	B^{EPSC}	C^{EPSC}
EPSC	Basal	8	10	180	30			
	Prismatic	92	10	2000	30			
	Pyramidal <a+c>	102	40	5000	65			
	Tensile Twin	40	15	70	50	0.01	0.98	5

4.2 Refinement of slip/twin parameters via CPFE model

Using the EPSC-identified constitutive parameters listed in Table 2, the parameters were further refined using the CPFE model. The refined parameters are listed in Table 3. The majority of the changes on the constitutive parameter compared with the EPSC-identified parameters are relevant to the initial and linear hardening terms, i.e., θ_0 and θ_1, respectively, to mitigate the faster strain hardening in the two regimes observed in the CPFE prediction shown in Figure 5. The other parameters of the extended Voce hardening law were kept same as used in the EPSC model, however, the ePTR model parameters were slightly adjusted to fit the measured twinning rate by the *in-situ* HEXRD (note that the ePTR model to better capture twinning rate will be discussed in Section 4.4 in detail). The CPFE predicted stress-strain curves using the refined constitutive parameters are shown in Figure 6 together with the EPSC-predicted and HEXRD-measured data already presented in Figure 5. The CPFE prediction results with the newly refined parameters are in excellent agreement with the experimental data even beyond the uniform elongation. In particular, the tensile instability is also well captured (Hereafter, the CPFE prediction refers the prediction results using the newly refined parameters).

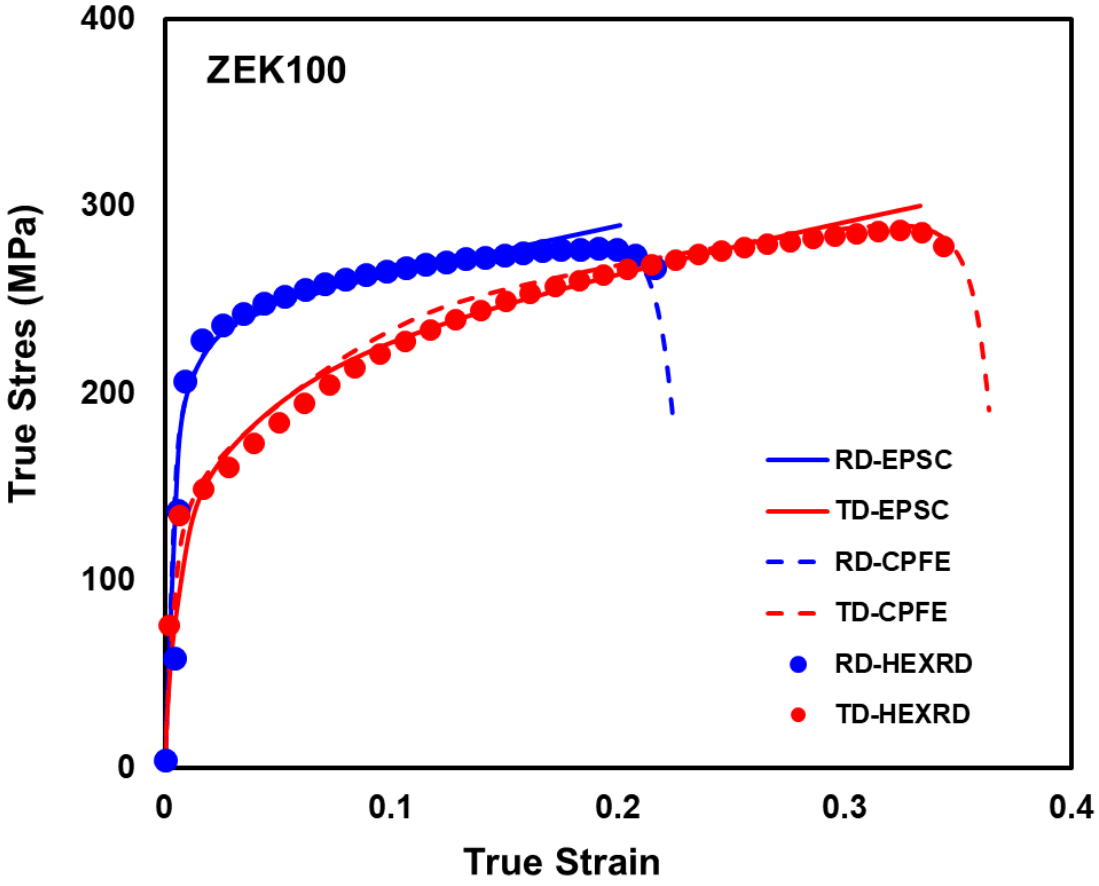

Figure 6. Stress-strain response of ZEK100 under uniaxial tension along the RD and TD: only CPFE results using the newly refined constitutive parameters for slip/twin systems were replaced from Figure 5.

Table 3 Refined constitutive parameters of slip/twin system for ZEK100 via CPFE

		Extended Voce parameters (Eq.(6))(*)				PTR parameters (Eq.(17))		
	Slip/Twin System	τ_0^{CPFE} (MPa)	τ_1^{CPFE} (MPa)	θ_0^{CPFE} (MPa)	θ_1^{CPFE} (MPa)	A^{CPFE}	B^{CPFE}	C^{CPFE}
CPFE	Basal	8	10	90	21			
	Prismatic	92	10	1000	21			
	Pyramidal <a+c>	102	40	2500	45.5			
	Tensile Twin	40	15	35	35	0.01	0.6	4

(* Hardening parameters were refined such that $\tau_0^{CPFE}=\tau_0^{EPSC}$, $\tau_1^{CPFE}=\tau_1^{EPSC}$, θ_0^{CPFE}=0.5·θ_0^{EPSC}, and θ_1^{CPFE}=0.7·θ_1^{EPSC})

The lattice strains of various lattice planes from the HEXRD experiments and the EPSC/CPFE simulations are shown in Figure 7. The lattice strains during the tension along the RD shown in Figure 7 (a) reveal that the both models reasonably well capture the lattice strain variation along the LD and TLD. In particular, the CPFE well predicts the gradual decrease of the lattice strain (in absolute value) beyond the localized necking. An interesting observation is that the CPFE-predictions slightly fluctuate during the deformation as observed in the HEXRD experiments, while the EPSC does not show such phenomena. The facts are consistent with the observation reported in Hu et al. (2017). As mentioned, the lattice strain is calculated for the grains whose *{hkil}* plane normal falls within an angular tolerance (here set as ±2°) along the measuring directions, i.e., LD or LTD. However, grains rotate during the deformation as aforementioned, and thus some grains can go in and out of the tolerance, consequently, lattice strain fluctuates. The CPFE model with its ability to consider the grain rotation by slip/twin activation can capture the lattice strain fluctuation as in the experiments. An exceptional lattice strain fluctuation of the {0002} lattice plane parallel to the TLD predicted by the EPSC model is relevant to the deformation twinning and corresponding re-orientation considered in the EPSC model although the amount of the twin is very small. Some grains reoriented after twinning such that their c-axis is almost parallel to the TLD, and they contribute to the lattice strain fluctuation.

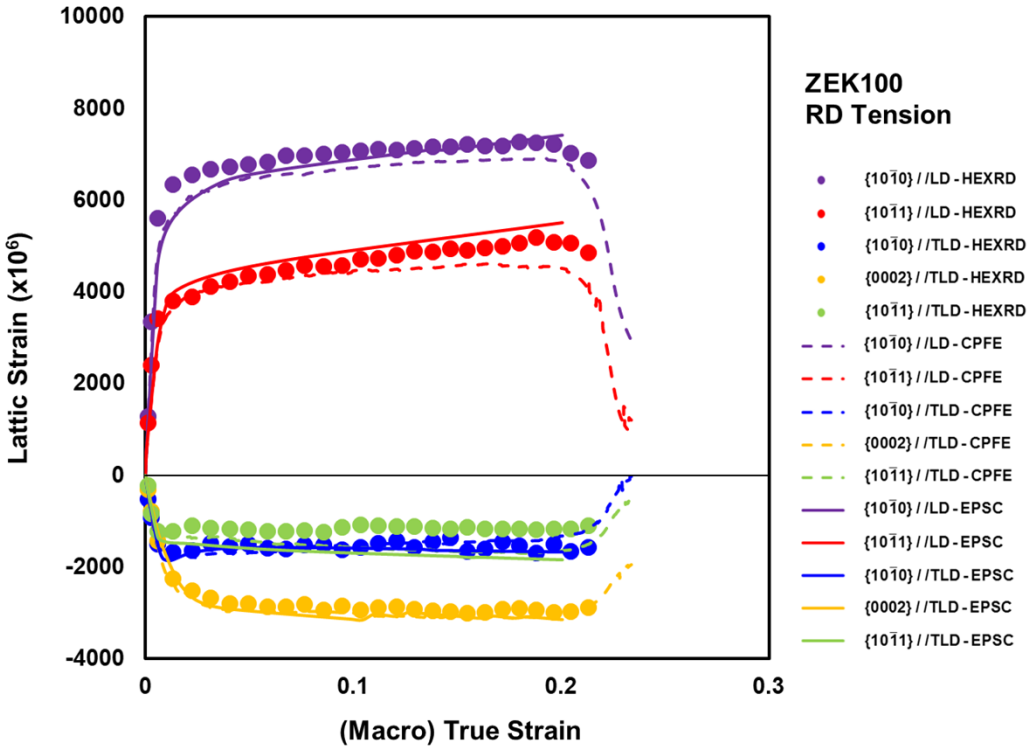

(a)

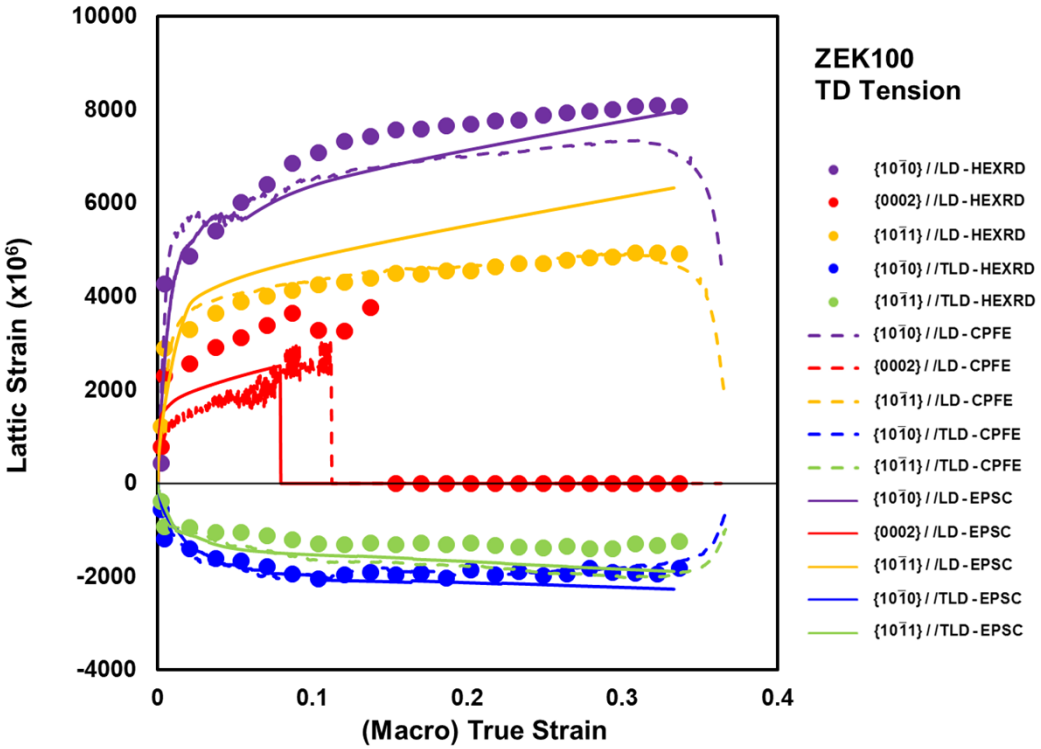

(b)

Figure 7. Lattice strain variations as a function of macroscopic strain measured by HEXRD, and predicted by EPSC/CPFE models under uniaxial tension along (a) the RD, and (b) the TD.

The comparisons of lattice strains during the tension along the TD are shown in Figure 7 (b). Both model predictions are in good agreement with the HEXRD data, however, the CPFE model better captures the experimental data, especially, lattice strain of $\{10\bar{1}1\}$ lattice plane whose normal is parallel to the LD. It is worthwhile to note that, experimentally, the lattice strain of {0002} planes along the LD beyond the strain of ~0.08 and ~0.11 for the EPSC and CPFE predictions, respectively, becomes zero because no more grain is within the tolerance. For the grain whose c-axis is (almost) parallel to the LD, i.e., TD of the sample, the most favorable deformation mode is the tensile twinning. The Schmid factor for the basal and prismatic slips is (nearly) zero, and the pyramidal slip is hard to occur due to its high CRSS. Therefore, the grain aligned in such way is gradually twinned and re-oriented. As a consequence, no grain is left within the tolerance at some point.

The crystal plasticity models can provide useful insights on the active slip and twin systems which govern the mechanical response during the deformation. The relative activity of m^{th} slip or twin modes is defined as follows:

$$\text{Relative Activity}^{m} = \frac{\sum_{\kappa=1}^{N^{mode}} \dot{\gamma}^{(\kappa)}}{\left(\sum_{\alpha=1}^{N^{SL}} \dot{\gamma}^{(\alpha)} + \sum_{\beta=1}^{N^{TW}} \dot{\gamma}^{(\beta)} \right)} \tag{22}$$

where N^{mode} (*mode* corresponds to basal, prismatic, pyramidal slips, and tensile twin) is the number of the slip or twin systems belonging to each mode.

The predicted relative activity vs. (macro) tensile strain plots by the EPSC and CPFE models during the tension along the RD and TD are shown in Figure 8 (a) and (b), respectively. During both loading conditions, the predicted relative activities of the basal slip and the tensile twinning by the two models are very similar qualitatively and quantitatively. However, the predicted relative activities of the non-basal slips, i.e., the prismatic and pyramidal slips, by the two models differ. The major difference is such that the prismatic slip is more activated, but pyramidal slip is less activated in the EPSC model compared with those in the CPFE model. In particular, EPSC model predicts that the pyramidal slip is inactive up to ~2% strain in the both loading directions. This is most likely caused by the treatment of the elastic-plastic behavior in the EPSC model. In the EPSC model, slip system is inactive ($\dot{\gamma}^{(\alpha)} = 0$) if resolved shear stress is less than $\tau_c^{(\alpha)}$ (Hutchinson, 1970). Owing to that, $\dot{\gamma}^{(\alpha)}$ of the pyramidal slip, exhibiting the highest CRSS ($\tau_0^{(\alpha)}$) among the available slip/twin systems, equals zero at the early stage of the loading and is less activated throughout the entire deformation. The less activation of the pyramidal slip is then compensated by the more activation of the prismatic slip. In contrast, according to Eq. (9), $\dot{\gamma}^{(\alpha)}$ is non-zero in the CPFE model even if resolved shear stress is less than $\tau_c^{(\alpha)}$, consequently, the pyramidal slip is activated from the commencement of the loading. Therefore, the higher macroscopic stress predicted by the CPFE than by the EPSC shown in Figure 5 is anticipated to the more activation of the pyramidal slip with the highest CRSS among the available slip/twin systems in the CPFE model[7].

[7] Another possible cause for the over-activation of the pyramidal slip in the CPFE can be the finite element type. It is well known that solid element with reduced integration (C3D8R) leads to over-constraints compared with the fully integrated solid element (C3D8), and thus, enhanced activity of the hard deformation mode, <c+a> pyramidal slip, can be predicted. To see how heavily the element type affects the activation of the hard deformation mode, FE simulations with cube-shaped FE model consists of 1,000 elements (10×10×10) with the two different element types were additionally conducted. Note that, for C3D8, each integration point represent a grain, and thus, 8 grains were assigned for an element. Although simulation with C3D8-type predicted the more activation of the pyramidal slip, the difference was negligible.

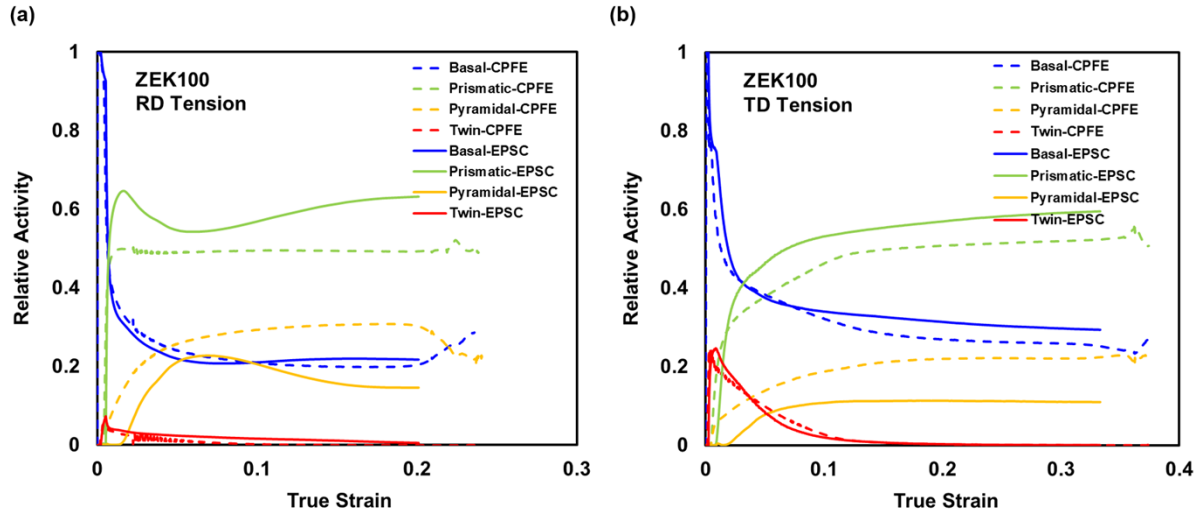

Figure 8. Relative activities of available slip/twin systems predicted EPSC and CPFE models under tension along (a) the RD and (b) the TD

The relative activity plot during tension along the RD shown in Figure 8 (a) reveals that the tensile twinning rarely occurs. Under such loading condition, the grains are oriented such that they are compressed along their c-axis (see Figure 2 (b)). Therefore, the tensile twinning is largely suppressed and most of deformation is accommodated by the slip. Since tensile twinning is inhibited, the compressive strain along the c-axis is likely to be accommodated by the pyramidal slip. In fact, the predicted results by the EPSC and CPFE models shown in Figure 8 (a) reveal that the pyramidal slip activity during tension along the RD is higher than that during tension along the TD as shown in Figure 8 (b). In contrast to the RD tension, noticeable activation of the tensile twinning is observed as shown in Figure 8 (b). For the grains with their c-axis parallel to the TD, the tensile deformation along the TD is predominantly accommodated by the tensile twin. The lower yield stress during tension along the TD compared to tension along the RD is anticipated to the more activation of the tensile twinning with lower CRSS at the early stage of the deformation. The gradual decrease of the tensile twin activity and increase of the pyramidal slip activity is a consequence of the grain re-orientation due to the tensile twinning. Once the grains, whose c-axis parallel to the TD, are re-oriented and lie along the RD, pyramidal slip is activated in those grains to accommodate the compressive strain along the RD. Such micromechanism leads to higher strain hardening over the deformation. Consequently, at strain ~0.3, the macroscopic stress ~280 MPa in the TD tension becomes comparable to that in the RD tension at strain ~0.2 (See Figure 6).

4.3 Texture evolution

The deformation texture was measured using the HEXRD following the same procedure used to measure the initial texture. For the *in-situ* HEXRD experiment, it was decided not to interrupt the tensile test for the texture measurement to avoid the stress relaxation effect. Therefore, texture information of the sample at the end of the tensile test was collected.

Predicted deformation textures using the EPSC and CPFE (with the newly identified parameters) models are compared in Figure 9 along with the HEXRD measured ones. The pole figures associated with the tension along the RD at ε~20%, Figure 9 (a)-(c), and the tension along the TD at ε~30%, Figure 9 (d)-(f), are plotted with the ranges of 0-4.5.

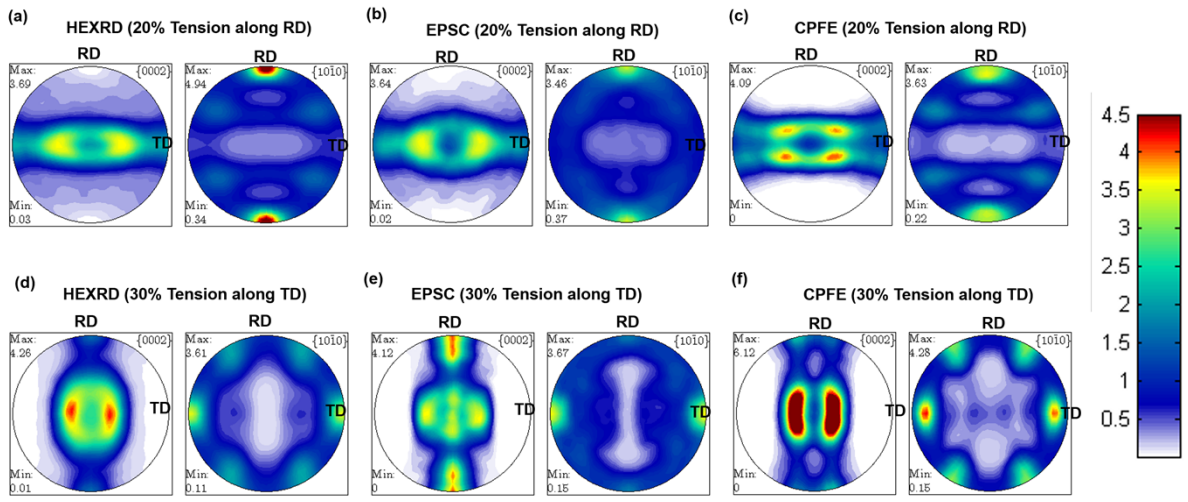

Figure 9. Deformed texture of ZEK100 after tension along RD at ε=20% (a) measured by HEXRD, (b) predicted by EPSC, and (c) predicted by CPFE, and after tension along TD at ε=30% (d) measured by HEXRD, (e) predicted by EPSC, and (f) predicted by CPFE.

The pole figures of the deformed sample measured by the HEXRD under the tension along the RD, shown in Figure 9 (a), reveal no noticeable texture change from the initial one, shown in Figure 2 (b). The EPSC (Figure 9 (b)) and CPFE (Figure 9 (c)) models both predict the deformed texture reasonably well, qualitatively and quantitatively. The results conclude that most of the deformation under such loading condition is accommodated by slips, and very little tensile twinning has occurred. Weaker prismatic plane peaks along the RD predicted by the EPSC compared with those measured by the HEXRD are anticipated to the disregard of the grain re-orientation associated with the slip, considering the negligible tensile twin activity under this loading condition. The CPFE well predicts the prismatic plane peaks along, but basal

peaks are off from the HEXRD measurement. It shows the separation of the two basal plane peaks ~20° off from the ND. Such prediction error is likely anticipated to the over-activation of the <c+a> pyramidal slip in the CPFE prediction as shown in Figure 8 (a). Furthermore, in the actual HEXRD measurement, the incident X-ray beam impinged the area outside of the neck in order to exclude the drastic texture change in the necking area. However, in the CPFE prediction, rigid body rotations occur inside the diffused necking region, and lead to the separation of the basal peaks.

Distinct behaviors are observed under the tension along the TD. HEXRD measured pole figures of the deformed sample in such loading condition, which are shown in Figure 9 (d), reveal that grains whose c-axes are (nearly or exactly) parallel to the TD rotate to lie along the RD. The EPSC and CPFE predictions, shown in Figure 9 (e) and (f), respectively, capture general texture changes observed from the HEXRD measurement with some discrepancies. Both CPFE and EPSC predict two basal poles ~20° off from the ND, but their intensities are lower and higher than the measurement, respectively. EPSC predicts basal plane peak along the ND, which is inconsistent with the measurement, and fails to capture the six prismatic plane peaks perpendicular to the ND. CPFE predicts the six prismatic plane peaks, but the basal plane peaks parallel to the RD are slightly off from the measurement. Again, the reason for the difference is most likely to the two major facts: (a) the EPSC scheme used in this study does not account for the slip-associated grain re-orientation, and (b) over-activation of the <c+a> slip in the CPFE prediction.

4.4 Discussion on the PTR model

The PTR model is further discussed in this subsection. According to the original PTR model in Eq. (15), as more grains are fully twinned, F_E increases faster than F_R, and the threshold value of twin fraction f_{cr} increases. Therefore, further twinning is inhibited until F_R catches up, and such mechanism is expressed as "self-controlling twinning". The parameter A controls the twinning rate during the early deformation stage, and the parameter B controls the twinning rate from the middle of the deformation as grains start to be fully twinned. Although the model has been employed in various approaches and constitutive models to characterize the twinning kinematics in HCP metals (Ardeljan et al., 2016; Liu et al., 2017; Ma et al., 2017; Wang et al., 2013; Wang et al., 2012a, 2012b), there has not been any direct comparison or thorough validation of the model predictions in terms of the twinning rate with the actual measurement.

In the current works, the actual twinning rate could be indirectly inferred by analyzing a basal plane peak intensity along the LD (here tensile loading along the TD) from the *in-situ* HEXRD measurements, and be compared with the PTR model predictions.

The HEXRD measured and EPSC/CPFE predicted normalized peak intensity (i.e., the peak intensity divided by the initial one before the deformation) of grains whose basal plane normal is parallel to the LD (here along the TD) are compared in Figure 10. Figure 10 (a) shows the normalized peak intensity from the HEXRD measurement and the EPSC predictions as a function of macro strain. Experimentally, the normalized peak intensity decreases gradually and becomes zero at the tensile strain of ~0.15.

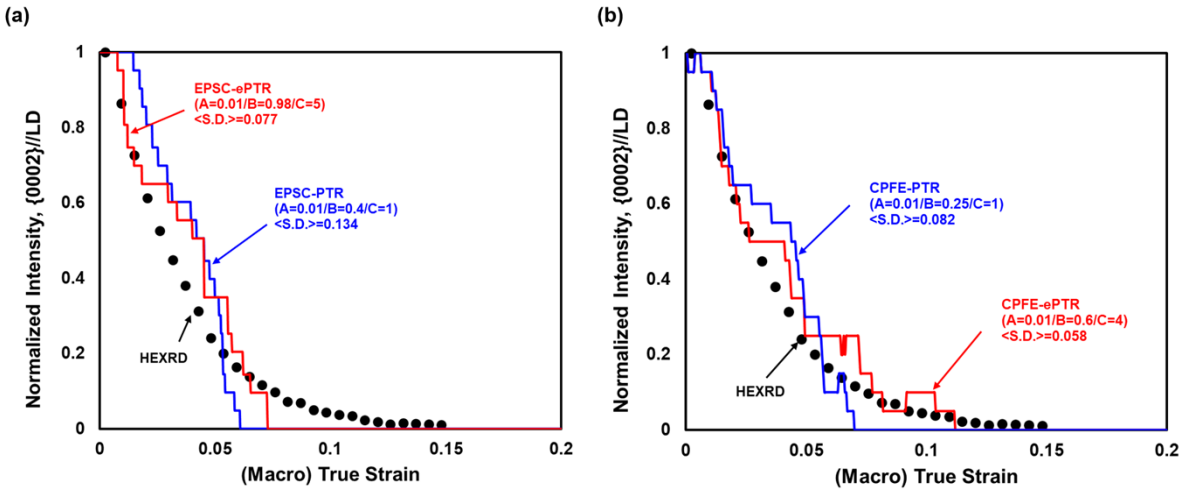

Figure 10. Normalized intensity of grains, whose {0002} plane normal is parallel to the LD during tension along the TD (a) HEXRD measurement vs. EPSC prediction, and (b) HEXRD measurement vs. CPFE prediction

For the EPSC models, two sets of PTR parameters were assumed; (a) the best-fit[8] parameters using the original PTR model, A=0.01/ B=0.4, with C=1, and (b) the best-fit parameters using the ePTR model listed in Table 2, A=0.01/B=0.98/C=5. In fact, the original version of the PTR model was first employed at the onset of this study. Experimentally measured data shows that the deformation twinning commences simultaneously with the tensile loading. Therefore, very small value of A, initial f_{cr}, was assumed. Then, the parameters B was adjusted to reproduce

[8] The 'best-fit parameters' represent the parameter set which best reproduces the measured normalized intensity variation.

the measured intensity. However, it was realized that the original PTR model could not well reproduce the measured deformation twinning rate. The prediction result using the original PTR model coupled with the EPSC model shown Figure 10 (a) reveals that the original PTR model leads to an almost linear decrease of the intensity, which is equivalent to an almost constant twinning rate. This results in the rather early drop of the normalized intensity to zero at the tensile strain of ~0.06.

Based on this observations, an enhanced PTR model parameter C in Eq. (17) was proposed to reproduce the parabolic-shaped decrease of the intensity by offering flexibility of the twinning rate during deformation. Finally, as shown in Figure 10 (a), the ePTR model with the newly introduced parameter better captures the experimental results than the original PTR model. Numerically, the standard deviation of the normalized intensity is smaller for the ePTR model (0.077 vs. 0.134). The improvement is more pronounced in the CPFE predictions as shown in Figure 10 (b) in which two prediction results are presented: (a) the best-fit parameters using the original PTR model, A=0.01/B=0.25/C=1, and (b) the best-fit parameters using ePTR model, A=0.01/B=0.6, C=4. The modification reduces the standard deviation from 0.082 to 0.058. Therefore, the best fit could be obtained using CPFE and ePTR models. Again, the ePTR model, via the introduction of a single exponent term which does not require onerous extra works, could better reproduce the experimental data with higher curvature, i.e., faster twinning rate at the early stage and gradual decrease of twinning rate as the deformation proceeds.

5. Concluding remarks

In this study, the high-energy X-ray diffraction (HEXRD) was coupled with the crystal plasticity models to characterize the constitutive behaviors of the ZEK100 magnesium alloy. New crystal plasticity models for HCP metals, namely, elastic-plastic self-consistent (EPSC) and crystal plasticity finite element (CPFE) models, were developed with the incorporation of deformation twinning kinematics. The critical resolved shear stress (CRSS) and hardening parameters of available slip/twin systems were identified by fitting of stress-strain curves and lattice strains. Computationally efficient EPSC model was first utilized to identify the CRSS and hardening parameters. The EPSC-identified parameters were then employed in the CPFE as an initial guess and the simple refinement of the parameters for the CPFE was followed. The coupled EPSC and CPFE approach opened up the opportunity for computationally-efficient constitutive characterization of advanced multi-phase materials and materials with low-symmetric slip (and/or twin) systems. The existing predominant twin re-orientation (PTR)

model was further enhanced via the introduction of a single exponent term to precisely capture the twinning rate inferred from the *in-situ* HEXRD-measured intensity change. The predicted results from the EPSC and CPFE models were compared with the HEXRD data, and the following conclusions were reached:

- The *in-situ* HEXRD measurement permitted accurate constitutive modeling of the HCP-structured ZEK100 magnesium alloy.
- Adopting the EPSC-identified constitutive parameters for the available slip/twin systems resulted in higher tensile stress predictions by the CPFE model compared with those by the EPSC model in two regimes.
- The constitutive parameter adjustments for the CPFE model relevant to the two regimes of stress differential led to excellent agreement of stress-strain curve between the CPFE predictions and *in-situ* HEXRD measurements.
- The EPSC and CPFE models reasonable well predicted deformation texture change during the tension along the RD. Both models also captured the general deformation texture change induced by the deformation twinning occurred during the tension along the TD.
- Utilizing the basal plane peak intensity data measured by the *in-situ* HEXRD, the ePTR model was proposed. The new model reduced the prediction error markedly compared with the existing PTR model, in particular, during the latter part of the twin deformation.
- The uniqueness of the constitutive parameters for the various slip/twin systems was underpinned by the agreement of the (macroscopic) stress-strain curves, (microscopic) lattice strains, twinning rate, and development of texture.

Acknowledgments

This work was supported by the U.S. Department of Energy (DOE) under Cooperative Agreement Number DE-EE0007756, with the United States Automotive Materials Partnership LLC (USAMP). H. J. Bong also appreciates the supports by the Fundamental Research Program of the Korea Institute of Materials Science (KIMS, PNK5650). This research used resources of the Advanced Photon Source (APS), a U.S. DOE Office of Science User Facility operated for the DOE Office of Science by Argonne National Laboratory under Contract No. DE-AC02-06CH11357. Oak Ridge National Laboratory is operated by UT-Battelle, LLC, for the U.S. DOE under contract DE-AC05-00OR22725.

Disclaimer

References

ABAQUS, 2011. 6.11 Analysis User's Manual. Providence, RI, USA.

Abdolvand, H., Daymond, M.R., Mareau, C., 2011. Incorporation of twinning into a crystal plasticity finite element model: Evolution of lattice strains and texture in Zircaloy-2. Int. J. Plast. 27, 1721–1738. https://doi.org/http://dx.doi.org/10.1016/j.ijplas.2011.04.005

Abedini, A., Butcher, C., Nemcko, M.J., Kurukuri, S., Worswick, M.J., 2017. Constitutive characterization of a rare-earth magnesium alloy sheet (ZEK100-O) in shear loading: Studies of anisotropy and rate sensitivity. Int. J. Mech. Sci. 128–129, 54–69. https://doi.org/https://doi.org/10.1016/j.ijmecsci.2017.04.013

Agnew, S.R., Brown, D.W., Tomé, C.N., 2006. Validating a polycrystal model for the elastoplastic response of magnesium alloy AZ31 using in situ neutron diffraction. Acta Mater. 54, 4841–4852. https://doi.org/https://doi.org/10.1016/j.actamat.2006.06.020

Agnew, S.R., Mulay, R.P., Polesak, F.J., Calhoun, C.A., Bhattacharyya, J.J., Clausen, B., 2013. In situ neutron diffraction and polycrystal plasticity modeling of a Mg–Y–Nd–Zr alloy: Effects of precipitation on individual deformation mechanisms. Acta Mater. 61, 3769–3780. https://doi.org/https://doi.org/10.1016/j.actamat.2013.03.010

Agnew, S.R., Singh, A., Calhoun, C.A., Mulay, R.P., Bhattacharyya, J.J., Somekawa, H., Mukai, T., Clausen, B., Wu, P.D., 2018. In-situ neutron diffraction of a quasicrystal-containing Mg alloy interpreted using a new polycrystal plasticity model of hardening due to {10.2} tensile twinning. Int. J. Plast. 100, 34–51. https://doi.org/https://doi.org/10.1016/j.ijplas.2017.09.005

Agnew, S.R., Tomé, C.N., Brown, D.W., Holden, T.M., Vogel, S.C., 2003. Study of slip mechanisms in a magnesium alloy by neutron diffraction and modeling. Scr. Mater. 48, 1003–1008. https://doi.org/https://doi.org/10.1016/S1359-6462(02)00591-2

Al-Samman, T., Li, X., 2011. Sheet texture modification in magnesium-based alloys by selective rare earth alloying. Mater. Sci. Eng. A 528, 3809–3822. https://doi.org/https://doi.org/10.1016/j.msea.2011.01.080

Ardeljan, M., Beyerlein, I.J., McWilliams, B.A., Knezevic, M., 2016. Strain rate and temperature sensitive multi-level crystal plasticity model for large plastic deformation behavior: Application to AZ31 magnesium alloy. Int. J. Plast. 83, 90–109. https://doi.org/http://dx.doi.org/10.1016/j.ijplas.2016.04.005

Boba, M., 2014. Warm Forming Behavior of ZEK100 and AZ31B Magnesum Alloy Sheet. UWSpace.

Bohlen, J., Nürnberg, M.R., Senn, J.W., Letzig, D., Agnew, S.R., 2007. The texture and anisotropy of magnesium–zinc–rare earth alloy sheets. Acta Mater. 55, 2101–2112. https://doi.org/https://doi.org/10.1016/j.actamat.2006.11.013

Bong, H.J., 2017. Forming Limit Diagram Prediction for Ultra-Thin Ferritic Stainless Steel Using Crystal Plasticity Finite Element Method. Trans. Mater. Process. 26, 144–149.

Bong, H.J., Barlat, F., Ahn, D.C., Kim, H.-Y., Lee, M.-G., 2013. Formability of austenitic and ferritic stainless steels at warm forming temperature. Int. J. Mech. Sci. 75, 94–109. https://doi.org/10.1016/j.ijmecsci.2013.05.017

Bong, H.J., Leem, D., Lee, J., Ha, J., Lee, M.-G., 2018. A Coupled Crystal Plasticity and Anisotropic Yield Function Model to Identify the Anisotropic Plastic Properties and Friction Behavior of an AA 3003 Alloy. Metall. Mater. Trans. A 49, 282–294. https://doi.org/10.1007/s11661-017-4406-1

Bong, H.J., Lim, H., Lee, M.-G., Fullwood, D.T., Homer, E.R., Wagoner, R.H., 2017. An RVE procedure for micromechanical prediction of mechanical behavior of dual-phase steel. Mater. Sci. Eng. A 695, 101–111. https://doi.org/https://doi.org/10.1016/j.msea.2017.04.032

Brown, D.W., Agnew, S.R., Abeln, S.P., Blumenthal, W.R., Bourke, M.A.M., Mataya, M.C., Tomé, C., Vogel, S.C., 2005. The Role of Texture, Temperature and Strain Rate in the Activity of Deformation Twinning . Mater. Sci. Forum 495–497, 1037–1042. https://doi.org/10.4028/www.scientific.net/MSF.495-497.1037

Chin, G.Y., Hosford, W.F., Mendorf, D.R., 1969. Accommodation of constrained deformation in f. c. c. metals by slip and twinning. Proc. R. Soc. London. A. Math. Phys. Sci. 309, 433 LP-456.

Cong, Z.H., Jia, N., Sun, X., Ren, Y., Almer, J., Wang, Y.D., 2009. Stress and strain partitioning of ferrite and martensite during deformation. Metall. Mater. Trans. A Phys. Metall. Mater. Sci. 40, 1383–1387. https://doi.org/10.1007/s11661-009-9824-2

Edwards, P.M., 2002. Origin 7.0: Scientific Graphing and Data Analysis Software. J. Chem. Inf. Comput. Sci. 42, 1270–1271. https://doi.org/10.1021/ci0255432

Eshelby, J.D., 1957. The Determination of the Elastic Field of an Ellipsoidal Inclusion, and Related Problems. Proc. R. Soc. London. Ser. A. Math. Phys. Sci. 241, 376 LP-396.

Gan, W., Bong, H.J., Lim, H., Boger, R.K., Barlat, F., Wagoner, R.H., 2017. Mechanism of the Bauschinger effect in Al-Ge-Si alloys. Mater. Sci. Eng. A 684, 353–372. https://doi.org/https://doi.org/10.1016/j.msea.2016.12.020

Gharghouri, M.A., Weatherly, G.C., Embury, J.D., Root, J., 1999. Study of the mechanical properties of Mg-7.7at.% Al by in-situ neutron diffraction. Philos. Mag. A 79, 1671–1695. https://doi.org/10.1080/01418619908210386

Gnäupel-Herold, T., 2009. Techniques for Neutron Stress Determination with High Spatial Resolution. J. Nondestruct. Eval. 28, 149. https://doi.org/10.1007/s10921-009-0057-5

Govik, A., Rentmeester, R., Nilsson, L., 2014. A study of the unloading behaviour of dual phase steel. Mater. Sci. Eng. A 602, 119–126. https://doi.org/10.1016/j.msea.2014.02.069

Guo, X.Q., Chapuis, A., Wu, P.D., Agnew, S.R., 2015. On twinning and anisotropy in rolled Mg alloy AZ31 under uniaxial compression. Int. J. Solids Struct. 64–65, 42–50. https://doi.org/https://doi.org/10.1016/j.ijsolstr.2015.03.012

Ha, J., Lee, J., Kim, J.H., Barlat, F., Lee, M.-G., 2014. Meso-Scopic Analysis of Strain Path Change Effect on the Hardening Behavior of Dual-Phase Steel. steel Res. Int. 85, 1047–1057. https://doi.org/10.1002/srin.201300186

Habib, S.A., Khan, A.S., Gnäupel-Herold, T., Lloyd, J.T., Schoenfeld, S.E., 2017. Anisotropy, tension-compression asymmetry and texture evolution of a rare-earth-containing magnesium alloy sheet, ZEK100, at different strain rates and temperatures: Experiments and modeling. Int. J. Plast. 95, 163–190. https://doi.org/https://doi.org/10.1016/j.ijplas.2017.04.006

Hammersley, A.P., 2004. FIT2D V12. 012 Reference Manual V6. 0, ESRF International Report No. ESRF98HA01T, Program avaiable at http://www.esrf.eu/computing/scientific/FIT2D.

Hielscher, R., Schaeben, H., 2008. A novel pole figure inversion method: specification of the MTEX algorithm. J. Appl. Crystallogr. 41, 1024–1037. https://doi.org/10.1107/S0021889808030112

Hu, X., Choi, K.S., Sun, X., Ren, Y., Wang, Y., 2016. Determining Individual Phase Flow Properties in a Quench and Partitioning Steel with In Situ High-Energy X-Ray Diffraction and Multiphase Elasto-Plastic Self-Consistent Method. Metall. Mater. Trans. A 47, 5733–5749. https://doi.org/10.1007/s11661-016-3373-2

Hu, X.H., Sun, X., Hector Jr., L.G., Ren, Y., 2017. Individual phase constitutive properties of a TRIP-assisted QP980 steel from a combined synchrotron X-ray diffraction and crystal plasticity approach. Acta Mater. 132, 230–244. https://doi.org/https://doi.org/10.1016/j.actamat.2017.04.028

Hu, X.H., Sun, X., Ren, Y., 2018. Examination of individual phase textures from HEXRD measurement and deformation anisotropy of a QP980 steel. Prep.

Hutchinson, J.W., 1970. Elastic-plastic behaviour of polycrystalline metals and composites. Proc. R. Soc. London. A. Math. Phys. Sci. 319, 247 LP-272.

Jia, N., Cong, Z.H., Sun, X., Cheng, S., Nie, Z.H., Ren, Y., Liaw, P.K., Wang, Y.D., 2009. An in situ high-energy X-ray diffraction study of micromechanical behavior of multiple phases in advanced high-strength steels. Acta Mater. 57, 3965–3977. https://doi.org/10.1016/j.actamat.2009.05.002

Jiang, L., Jonas, J.J., Mishra, R., 2011. Effect of dynamic strain aging on the appearance of the rare earth texture component in magnesium alloys. Mater. Sci. Eng. A 528, 6596–6605. https://doi.org/https://doi.org/10.1016/j.msea.2011.05.027

Kada, S.R., Lynch, P.A., Barnett, M.R., 2015. Development of a laboratory-based transmission diffraction technique for {\it in situ} deformation studies of Mg alloys. J. Appl. Crystallogr. 48, 365–376. https://doi.org/10.1107/S1600576715001879

Kada, S.R., Lynch, P.A., Kimpton, J.A., Barnett, M.R., 2016. In-situ X-ray diffraction studies of slip and twinning in the presence of precipitates in AZ91 alloy. Acta Mater. 119, 145–156. https://doi.org/https://doi.org/10.1016/j.actamat.2016.08.022

Kalidindi, S.R., 1998. Incorporation of deformation twinning in crystal plasticity models. J. Mech. Phys. Solids 46, 267–290. https://doi.org/http://dx.doi.org/10.1016/S0022-5096(97)00051-3

Kalidindi, S.R. (Surya R., 1992. Polycrystal plasticity : constitutive modeling and deformation processing. Massachusetts Institute of Technology.

Kalidindi, S.R., Bronkhorst, C.A., Anand, L., 1992. Crystallographic texture evolution in bulk deformation processing of FCC metals. J. Mech. Phys. Solids 40, 537–569. https://doi.org/10.1016/0022-5096(92)80003-9

Kim, H.S., Sumption, M.D., Bong, H.J., Lim, H., Collings, E.W., 2017. Development of a multi-scale simulation model of tube hydroforming for superconducting RF cavities. Mater. Sci. Eng. A 679, 104–115. https://doi.org/https://doi.org/10.1016/j.msea.2016.10.022

Kurukuri, S., Worswick, M.J., Bardelcik, A., Mishra, R.K., Carter, J.T., 2014. Constitutive Behavior of Commercial Grade ZEK100 Magnesium Alloy Sheet over a Wide Range of Strain Rates. Metall. Mater. Trans. A 45, 3321–3337. https://doi.org/10.1007/s11661-014-2300-7

Lee, J., Kim, S.-J., Lee, Y.-S., Lee, J.-Y., Kim, D., Lee, M.-G., 2017. Distortional hardening concept for modeling anisotropic/asymmetric plastic behavior of AZ31B magnesium alloy sheets. Int. J. Plast. 94, 74–97. https://doi.org/http://dx.doi.org/10.1016/j.ijplas.2017.02.002

Lentz, M., Klaus, M., Coelho, R.S., Schaefer, N., Schmack, F., Reimers, W., Clausen, B., 2014. Analysis of the Deformation Behavior of Magnesium-Rare Earth Alloys Mg-2 pct Mn-1 pct Rare Earth and Mg-5 pct Y-4 pct Rare Earth by In Situ Energy-Dispersive X-ray Synchrotron Diffraction and Elasto-Plastic Self-Consistent Modeling. Metall. Mater. Trans. A 45, 5721–5735. https://doi.org/10.1007/s11661-014-2533-5

Lentz, M., Klaus, M., Wagner, M., Fahrenson, C., Beyerlein, I.J., Zecevic, M., Reimers, W., Knezevic, M., 2015. Effect of age hardening on the deformation behavior of an Mg–Y–Nd alloy: In-situ X-ray diffraction and crystal plasticity modeling. Mater. Sci. Eng. A 628, 396–409. https://doi.org/https://doi.org/10.1016/j.msea.2015.01.069

Lim, H., Jong Bong, H., Chen, S.R., Rodgers, T.M., Battaile, C.C., Lane, J.M.D., 2018. Developing anisotropic yield models of polycrystalline tantalum using crystal plasticity finite element simulations. Mater. Sci. Eng. A 730, 50–56. https://doi.org/https://doi.org/10.1016/j.msea.2018.05.096

Liu, C., Shanthraj, P., Diehl, M., Roters, F., Dong, S., Dong, J., Ding, W., Raabe, D., 2018. An integrated crystal plasticity–phase field model for spatially resolved twin nucleation, propagation, and growth in hexagonal materials. Int. J. Plast. 106, 203–227. https://doi.org/https://doi.org/10.1016/j.ijplas.2018.03.009

Liu, Q., Roy, A., Silberschmidt, V. V, 2017. Temperature-dependent crystal-plasticity model for magnesium: A bottom-up approach. Mech. Mater. 113, 44–56. https://doi.org/https://doi.org/10.1016/j.mechmat.2017.07.008

Liu, Y., Wei, Y., 2014. A polycrystal based numerical investigation on the temperature dependence of slip resistance and texture evolution in magnesium alloy AZ31B. Int. J. Plast. 55, 80–93. https://doi.org/https://doi.org/10.1016/j.ijplas.2013.09.011

Ma, C., Chapuis, A., Guo, X., Zhao, L., Wu, P., Liu, Q., Mao, X., 2017. Modeling the deformation behavior of a rolled Mg alloy with the EVPSC-TDT model. Mater. Sci. Eng. A 682, 332–340. https://doi.org/http://dx.doi.org/10.1016/j.msea.2016.11.027

Muhammad, W., Mohammadi, M., Kang, J., Mishra, R.K., Inal, K., 2015. An elasto-plastic constitutive model for evolving asymmetric/anisotropic hardening behavior of AZ31B and ZEK100 magnesium alloy sheets considering monotonic and reverse loading paths. Int. J. Plast. 70, 30–59. https://doi.org/https://doi.org/10.1016/j.ijplas.2015.03.004

Muránsky, O., Carr, D.G., Barnett, M.R., Oliver, E.C., Šittner, P., 2008. Investigation of deformation mechanisms involved in the plasticity of AZ31 Mg alloy: In situ neutron diffraction and EPSC modelling. Mater. Sci. Eng. A 496, 14–24. https://doi.org/https://doi.org/10.1016/j.msea.2008.07.031

Muránsky, O., Carr, D.G., Šittner, P., Oliver, E.C., 2009. In situ neutron diffraction investigation of deformation twinning and pseudoelastic-like behaviour of extruded AZ31 magnesium alloy. Int. J. Plast. 25, 1107–1127. https://doi.org/http://dx.doi.org/10.1016/j.ijplas.2008.08.002

Neil, C.J., Wollmershauser, J.A., Clausen, B., Tomé, C.N., Agnew, S.R., 2010. Modeling lattice strain evolution at finite strains and experimental verification for copper and stainless steel using in situ neutron diffraction. Int. J. Plast. 26, 1772–1791. https://doi.org/https://doi.org/10.1016/j.ijplas.2010.03.005

Nemcko, M.J., Abedini, A., Butcher, C., Wu, P., Worswick, M.J., 2017. Microstructural and Numerical Investigation on the Shear Response of a Rare-Earth Magnesium Alloy Sheet BT - Magnesium Technology 2017, in: Solanki, K.N., Orlov, D., Singh, A., Neelameggham, N.R. (Eds.), . Springer International Publishing, Cham, pp. 477–482.

Proust, G., Tomé, C.N., Jain, A., Agnew, S.R., 2009. Modeling the effect of twinning and detwinning during strain-path changes of magnesium alloy AZ31. Int. J. Plast. 25, 861–880. https://doi.org/https://doi.org/10.1016/j.ijplas.2008.05.005

Qiao, H., Agnew, S.R., Wu, P.D., 2015. Modeling twinning and detwinning behavior of Mg alloy ZK60A during monotonic and cyclic loading. Int. J. Plast. 65, 61–84. https://doi.org/https://doi.org/10.1016/j.ijplas.2014.08.010

Qiao, H., Guo, X.Q., Oppedal, A.L., El Kadiri, H., Wu, P.D., Agnew, S.R., 2017. Twin-induced hardening in extruded Mg alloy AM30. Mater. Sci. Eng. A 687, 17–27. https://doi.org/https://doi.org/10.1016/j.msea.2016.12.123

Qiao, H., Wu, P.D., Guo, X.Q., Agnew, S.R., 2016. A new empirical equation for termination of twinning in magnesium alloys. Scr. Mater. 120, 71–75. https://doi.org/https://doi.org/10.1016/j.scriptamat.2016.04.015

Singh, J., Kim, M.-S., Choi, S.-H., 2018. The effect of initial texture on micromechanical deformation behaviors in Mg alloys under a mini-V-bending test. Int. J. Plast. https://doi.org/https://doi.org/10.1016/j.ijplas.2018.01.008

Staroselsky, A.V., 1998. Crystal plasticity due to slip and twinning. Massachusetts Institute of Technology.

Sun, X., Choi, K.S., Liu, W.N., Khaleel, M.A., 2009. Predicting failure modes and ductility of dual phase steels using plastic strain localization. Int. J. Plast. 25, 1888–1909. https://doi.org/10.1016/j.ijplas.2008.12.012

Tadano, Y., Yoshihara, Y., Hagihara, S., 2016. A crystal plasticity modeling considering volume fraction of deformation twinning. Int. J. Plast. 84, 88–101. https://doi.org/http://dx.doi.org/10.1016/j.ijplas.2016.05.002

Tomé, C.N., Lebensohn, R.A., Kocks, U.F., 1991. A model for texture development dominated by deformation twinning: Application to zirconium alloys. Acta Metall. Mater. 39, 2667–2680. https://doi.org/http://dx.doi.org/10.1016/0956-7151(91)90083-D

Turner, P.A., Tomé, C.N., 1994. A study of residual stresses in Zircaloy-2 with rod texture. Acta Metall. Mater. 42, 4143–4153. https://doi.org/https://doi.org/10.1016/0956-7151(94)90191-0

Wang, H., Clausen, B., Capolungo, L., Beyerlein, I.J., Wang, J., Tomé, C.N., 2016. Stress and strain relaxation in magnesium AZ31 rolled plate: In-situ neutron measurement and elastic viscoplastic polycrystal modeling. Int. J. Plast. 79, 275–292. https://doi.org/https://doi.org/10.1016/j.ijplas.2015.07.004

Wang, H., Clausen, B., Tomé, C.N., Wu, P.D., 2013a. Studying the effect of stress relaxation and creep on lattice strain evolution of stainless steel under tension. Acta Mater. 61, 1179–1188. https://doi.org/https://doi.org/10.1016/j.actamat.2012.10.027

Wang, H., Raeisinia, B., Wu, P.D., Agnew, S.R., Tomé, C.N., 2010a. Evaluation of self-consistent polycrystal plasticity models for magnesium alloy AZ31B sheet. Int. J. Solids Struct. 47, 2905.

Wang, H., Wu, P., Kurukuri, S., Worswick, M.J., Peng, Y., Tang, D., Li, D., 2018. Strain rate sensitivities of deformation mechanisms in magnesium alloys. Int. J. Plast. https://doi.org/https://doi.org/10.1016/j.ijplas.2018.04.005

Wang, H., Wu, P.D., Tomé, C.N., Huang, Y., 2010b. A finite strain elastic–viscoplastic self-consistent model for polycrystalline materials. J. Mech. Phys. Solids 58, 594.

Wang, H., Wu, P.D., Tomé, C.N., Wang, J., 2012b. Study of lattice strains in magnesium alloy AZ31 based on a large strain elastic-viscoplastic self-consistent polycrystal model. Int. J. Solids Struct. 49, 2155–2167. https://doi.org/http://dx.doi.org/10.1016/j.ijsolstr.2012.04.026

Wang, H., Wu, P.D., Tomé, C.N., Wang, J., 2012a. A constitutive model of twinning and detwinning for hexagonal close packed polycrystals. Mater. Sci. Eng. A 555, 93–98. https://doi.org/http://dx.doi.org/10.1016/j.msea.2012.06.038

Wang, H., Wu, P.D., Wang, J., 2013. Modeling inelastic behavior of magnesium alloys during cyclic loading–unloading. Int. J. Plast. 47, 49–64. https://doi.org/10.1016/j.ijplas.2013.01.007

Wang, H., Wu, P.D., Wang, J., Tomé, C.N., 2013b. A crystal plasticity model for hexagonal close packed (HCP) crystals including twinning and de-twinning mechanisms. Int. J. Plast. 49, 36–52. https://doi.org/http://dx.doi.org/10.1016/j.ijplas.2013.02.016

Wu, L., Agnew, S.R., Brown, D.W., Stoica, G.M., Clausen, B., Jain, A., Fielden, D.E., Liaw, P.K., 2008. Internal stress relaxation and load redistribution during the twinning–detwinning-dominated cyclic deformation of a wrought magnesium alloy, ZK60A. Acta Mater. 56, 3699–3707. https://doi.org/https://doi.org/10.1016/j.actamat.2008.04.006

Yoo, M.H., 1981. Slip, twinning, and fracture in hexagonal close-packed metals. Metall. Trans. A 12, 409–418.

Zhang, J., Joshi, S.P., 2012. Phenomenological crystal plasticity modeling and detailed micromechanical investigations of pure magnesium. J. Mech. Phys. Solids 60, 945–972. https://doi.org/http://dx.doi.org/10.1016/j.jmps.2012.01.005